

Abstract. We present ISO-LWS measurements of the main gas cooling lines, $[C^+]$ $158\mu\text{m}$ and $[O^0]$ $63\mu\text{m}$ towards a moderate opacity molecular cloud ($A_v \sim 3$), L1721, illuminated by the B2 star ν Sco ($\chi = 5-10$). These data are combined with an extinction map and IRAS dust emission images to test our understanding of gas heating and cooling in photo-dissociation regions (PDRs). This nearby PDR is spatially resolved in the IRAS images; variations in the IRAS colors across the cloud indicate an enhanced abundance of small dust grains within the PDR. A spatial correlation between the gas cooling lines and the infrared emission from small dust grains illustrates the dominant role of small dust grains in the gas heating through the photoelectric effect. The photoelectric efficiency, determined from the observations by ratioing the power radiated by gas and small dust grains, is in the range 2 to 3 % in close agreement with recent theoretical estimates (Bakes & Tielens, 1994; Weingartner & Draine, 2001). The brightness profiles across the PDR in the $[C^+]$ $158\mu\text{m}$ and $[O^0]$ $63\mu\text{m}$ lines are compared with model calculations where the density profile is constrained by the extinction data and where the gas chemical and thermal balances are solved at each position. We show that abundance variations of small dust grains across the PDR must be considered to account for the LWS observations.

Key words: ISM: clouds - ISM: dust, extinction - atomic processes - molecular processes - radiative transfer

Photoelectric effect on dust grains across the L1721 cloud in the ρ Ophiuchi molecular complex *

E. Habart¹, L. Verstraete¹, F. Boulanger¹, G. Pineau des Forêts¹, F. Le Peintre¹ and J.P. Bernard¹

Institut d'Astrophysique Spatiale, Orsay, France

Received January 12 / accepted March 08, 2001

1. Introduction

The bulk of interstellar matter is found in regions of low to moderate opacity to UV and visible light where stellar radiation plays a dominant role in determining the chemical and thermal state of the gas. These photon-dominated or photo-dissociation regions have been the subject of many observations and theoretical studies over the past twenty years (Hollenbach & Tielens, 1999, for a review see). In the classical theoretical paradigm, a PDR is characterized by its proton density, n_H , and a scaling factor, χ , which normalises the incident radiation field to the Solar Neighbourhood radiation field in the far-ultraviolet. Comparison between observations and model calculations have concentrated on bright objects with high $\chi > 10^3$ and gas density $n_H > 10^3 \text{ cm}^{-3}$ which are the easiest to observe. The gain in sensitivity provided by the Infrared Space Observatory (ISO) for gas line observations now permits to extend these studies to less excited PDRs with lower n_H and χ which are the most widespread in the interstellar medium (ISM). Models show that in such PDRs the gas heating is dominated by the photoelectric effect on dust grains (Hollenbach et al., 1991; Le Boulot et al., 1993; Kemper et al., 1999). Photoelectric heating has been the subject of recent theoretical investigations which provide an estimate of the photoelectric yield as a function of grain size where the small grains (radius $\leq 100 \text{ \AA}$) dominate the overall photoelectric heating (Bakes & Tielens, 1994; Weingartner & Draine, 2001). It is thus in low excitation PDRs including the diffuse interstellar medium that one can most directly validate this theoretical understanding of a key physical process for the ISM, independently of other heating processes. Recently, Wolfire et al. (1995) have used the work of Bakes and Tielens (1994, hereafter BT) to compute the equilibrium thermal states of the diffuse atomic medium. For the Solar Neighbourhood, their

calculations give a net estimate of the $[\text{C}^+]$ $158\mu\text{m}$ line emission per hydrogen atom in agreement with the value derived from the comparison of the FIRAS and H I data at high Galactic latitude (Boulanger et al., 1996a). However, this validation of the BT work depends on the relative gas mass in the cold and warm phases of the ISM which is poorly constrained observationally.

In this paper, we investigate the photoelectric heating of the ISM through the study of a specific, low-excitation PDR. The comparison of the power radiated by gas and dust allows us to correlate the gas and dust emission and determine the photoelectric efficiency.

To carry out this study, we selected the Lynds Dark Nebula 1721 (Lynds, 1962, L1721,), a nearby molecular cloud in the ρ Ophiuchi region. This cloud as seen in the IRAS data has a roughly spherical geometry and a moderate opacity to stellar light ($A_v = 3$ at cloud center). It is heated on one side by the B2 star ν Sco and by a more isotropic interstellar radiation field created by the Upper Scorpius association. We present in this paper observations of the $[\text{C}^+]$ $158\mu\text{m}$ and $[\text{O}^0]$ $63\mu\text{m}$ lines obtained with the Long Wavelength Spectrometer (Clegg et al., 1996, LWS,) on board the Infrared Space Observatory (Kessler et al., 1996, ISO,). These observations are combined with IRAS images and an extinction map (Sects. 2-3). Thanks to its proximity to the Sun and the moderate gas density, the L1721 PDR is spatially resolved by both the gas and dust observations. The data is interpreted within the framework of a model of the gas emission (Sect. 3). The data allows us to determine the photoelectric efficiency and to illustrate the dominant role of small dust grains in the photoelectric heating (Sect. 4). The paper conclusions are summarised in Sect. 5.

2. Observations

The L1721 cloud is centered at $\alpha = 16\text{h } 14\text{m } 30.41\text{s}$ and $\beta = -18^\circ 58' 7.9''$ (Epoch 2000), at the north of the ρ Ophiuchi complex. The B2 star ν Sco is located at a distance of ~ 134 pc. The projected distance between the center of the cloud and the star is approximately 1.7 pc. We discuss in detail the incident radiation field of L1721 in Sect. 3.2.

Send offprint requests to: E. Habart (emilie.habart@ias.u-psud.fr)

* Based on observations with ISO, an ESA project with instruments funded by ESA Member States (especially the PI countries: France, Germany, the Netherlands and the United Kingdom) and with the participation of ISAS and NASA.



Fig. 1. *L1721 as seen in the IRAS data. Top: map of the sum of IRAS bands (12+25+60+100 μm) with the beams of LWS observations projected on sky. Bottom: map of the 12/100 μm IRAS band ratio. In this latter map, the limb brightening or halo of the cloud is clearly visible. The circles show the LWS beam in the cut taken across the cloud (20 positions) and the position of ν Sco is marked by a star.*

On the map of the 12/100 μm IRAS band ratio (see Fig. 1), the limb brightening of the cloud is clearly visible. Former studies have shown that ratios of the different IRAS bands mostly trace dust abundance variations (Boulanger et al., 1990; Bernard et al., 1993). We discuss the abundance variations of small grains across L1721 in Sect. 3.5.

2.1. Gas cooling lines



Fig. 2. *Intensities of the C^+ and O^0 lines with 3σ error bars as measured by LWS at each position across L1721. The background contribution has been subtracted (see text). The ν Sco star lies at the right end of the cut.*

The $[\text{O}^0]$ 63 μm and $[\text{C}^+]$ 158 μm lines have been observed by ISO with the LWS (TDT = 45401125, LWS02 grating mode, Clegg et al., 1996). At each sky position, the C^+ and O^0 lines have been observed 8 and 30 times respectively with 5 seconds-individual scans (the integration per grating point was 0.4 seconds). The resolution (FWHM) is $\Delta\lambda = 0.5$ and $0.29 \mu\text{m}$ for the C^+ and O^0 lines respectively and each resolution element was sampled twice. We use the LWS pipeline version 7 for standard data reduction. To remove glitches (cosmic ray impacts on the detectors), we co-add all scans to obtain a first estimate of the mean line spectrum. Subtracting this mean spectrum from each individual scan, we obtain a (noise + glitch) - spectrum in which glitches are identified as 3σ - and 5σ -outliers for C^+ and O^0 respectively. After rejection

of glitches, all scans are again co-added to produce the final line spectrum. Line fluxes and error bars are obtained by fitting a Gaussian and a linear baseline to the profiles. The Fig. 2 shows the line intensity profiles.

To measure the line emission from L1721, we need to subtract the contribution of the diffuse ISM along the line of sight. We express the background contribution to the line emission as:

$$I_b = Y \times \nu I_\nu \quad (1)$$

where Y is the line-to-continuum ratio and νI_ν the continuum brightness at the line wavelength. In the case of the C^+ line, we take the line-to-continuum ratio measured in the Galaxy at high latitude, $Y_{\text{C}^+} = 0.009 \pm 0.0015$ from Boulanger et al. (1996a). This value agrees well with the Galactic plane mean value of 0.0082 reported by Wright et al. (1991) based on the FIRAS (Far-Infrared Absolute Spectrophotometer) survey of the far-infrared emission from our Galaxy. Wright et al. (1991) observed, as expected theoretically, that the intensity of the C^+ line scales linearly with the dust continuum emission. The variations of the C^+ line-to-continuum ratio, due to differences in the dust properties, in the color of the ambient interstellar radiation field or the saturation of the C^+ cooling rate when the level populations are in equilibrium with dense warm gas, are within 25% in the plane of Galaxy. In the following we consider that $Y_{\text{C}^+} = 9 \pm 2.25 \cdot 10^{-3}$ in the proximity of the L1721 cloud. For the O^0 line, the combination of the observations of Caux & Gry (1997) in the diffuse ISM and the IRAS band at 60 μm provide a large range of Y_{O^0} values from $5 \cdot 10^{-4}$ to $5 \cdot 10^{-3}$. To derive the O^0 background around the L1721 cloud we take the median of these values $Y_{\text{O}^0} = 1.7 \cdot 10^{-3}$. Note however that the large uncertainty on Y_{O^0} will not affect our estimate of the O^0 line emission in the L1721 cloud because the contribution of the diffuse ISM to the O^0 emission along the line of sight is much lower than the line intensity in the cloud. For the continuum brightness, we use the DIRBE (Diffuse Infrared Background Experiment) data corrected for zodiacal light. The continuum values are found from the average of DIRBE points in the diffuse ISM around the L1721 cloud. The variations of the DIRBE values are typically within 20% in the surrounding of the cloud. We find: $\nu I_\nu(158 \mu\text{m}) = 9.2 \pm 1.9 \cdot 10^{-4}$ ergs/s/cm²/sr and $\nu I_\nu(60 \mu\text{m}) = 3.4 \pm 0.7 \cdot 10^{-4}$ ergs/s/cm²/sr. The corresponding background emission values which have been subtracted from our LWS cut are $8.3 \pm 2.7 \cdot 10^{-6}$ and $5.8 \pm 1.2 \cdot 10^{-7}$ ergs/s/cm²/sr for C^+ and O^0 respectively.

2.2. Dust infrared emission

Fig. 3 shows the background subtracted surface brightness in the four IRAS bands. For each IRAS band, the background emission has been estimated along cuts extending the LWS cut at both ends of the cloud. The background emission is taken to be the average of the minimum values of these extended cuts: $I_{12}^b = 1.2 \pm 0.2$, $I_{25}^b = 1.8 \pm 0.3$, $I_{60}^b =$



Fig. 3. Surface brightness in the 4 IRAS bands as a function of the observed LWS positions. The background emission has been subtracted (see Sect. 2.2).

7 ± 1.6 and $I_{100}^b = 35 \pm 3.9$ MJy/sr.

The IRAS and COBE data are well explained with dust models comprising three components (Désert et al., 1990; Dwek et al., 1997). We adopt the Désert et al. model: the three dust components are thus by order of increasing sizes (in terms of the grain radius, a):

1. large aromatic molecules or PAHs (Polycyclic Aromatic Hydrocarbons) which contribute most of the 12 μm band ($a = 4$ to 12 \AA)
2. the Very Small Grains (VSGs) which dominate the 25 μm and 60 μm bands ($a = 12$ to 150 \AA)
3. the Big Grains (BGs) which make most of the 100 μm band ($a = 1.5 \cdot 10^{-2}$ to 0.11 μm).

In the following, we will often refer to PAHs and VSGs as the *small dust grain* populations. To derive the photoelectric efficiency for each grain component, we need to decompose the total infrared (IR) emission into individual dust contributions at each position in the cloud.

In the case of PAHs, we use the following relationship based on ISOCAM and DIRBE data (Boulanger et al., 1996b; Bernard et al., 1994):

$$I_{PAH} = 1.5 \times \nu I_\nu(12 \mu\text{m}) \text{ erg cm}^{-2} \text{ s}^{-1} \text{ sr}^{-1}.$$

The emission of big grains is modelled with a modified blackbody of temperature T_{BG} and an emissivity law proportional to ν^2 . The value of T_{BG} is estimated using the flux measured by all ten LWS detectors covering the range $\lambda = 42.5\text{-}176 \mu\text{m}$. At each position, we fit the ten spectral points with the modified blackbody: a constant temperature of $T_{BG} = 20$ K at all positions is found to provide a satisfactory fit. Finally, this modified blackbody is scaled to match the 100 μm IRAS band.

For the VSGs emission, we first obtain two spectral points at 25 and 60 μm from:

$$I_{25,60}(VSG) = I_{25,60}(IRAS) - I_{25,60}(BG)$$

At each cloud position, we fit these two points with a modified blackbody of constant temperature $T_{VSG} = 70$ K and an emissivity law proportional to ν .

The bolometric intensity of each dust component is shown in Fig. 4: in fact, the VSGs and BGs emission pro-

files are quite similar to the 25+60 μm and 100 μm IRAS band profiles respectively. We note that BGs and VSGs temperatures are expected to decrease as one penetrates into the cloud. The constant temperature we find may be due to the spherical geometry of the cloud where warm and cold dust are mixed along a given line of sight.

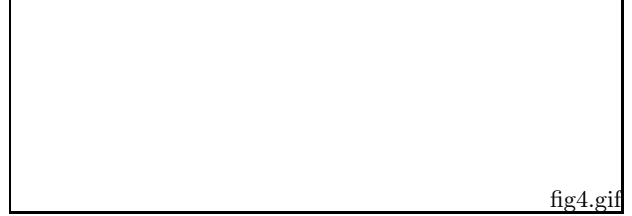


Fig. 4. Integrated flux of each dust component as a function of the position along the LWS cut. ν Sco lies at the right end of the cut.

3. Modelling the gas line cooling

To study the photoelectric effect on dust grains across this nearby PDR, we will compare the total gas cooling lines to the dust IR emission (see Sect. 4). In the case of low excitation PDRs, cooling by the pure rotational lines of H_2 may be important. As this latter has not been observed, we resort to an updated version of the PDR model described in Le Bourlot et al. (1993) to estimate the cooling by H_2 . Moreover the comparison between the brightness profiles observed across the L1721 PDR in the $[\text{C}^+]$ 158 μm and $[\text{O}^0]$ 63 μm lines with model calculations provides a test for our understanding of gas heating/cooling in PDRs. The key ingredients of this model are the density profile across the PDR and the incident radiation field at the cloud surface. In the following, we describe how these quantities are constrained in order to produce a realistic model of the L1721 PDR.

3.1. The density distribution

To determine the density profile of L1721 we use a visual extinction map derived from star counts (Cambrésy, 1999). Fig. 5 displays the column density, $N_H = Av/(0.54 \times 10^{-21}) \text{ cm}^{-2}$ observed across L1721. The column density profile is well represented by a gas density distribution of the form (see Fig. 5):

$$n_H(r) = \begin{cases} n_H^0 \times (r/r_1)^{-1.9} & : r_1 < r \leq r_m \\ n_H^0 & : r \leq r_1 \end{cases} \quad (2)$$

with r the radial distance to the cloud center, $n_H^0 = 2915 \text{ cm}^{-3}$ the constant density in the $0 \leq r \leq r_1$ region with $r_1 = 0.2$ pc and $r_m = 2.2$ pc. In this derivation, we assume that R_v is constant and equal to 3.1 across the L1721 cloud. A higher value of R_v , 5.5, that is commonly observed in opaque cores, would multiply our extinction values by a small factor, about 1.12.



Fig. 5. Comparison of the column density observed (solid line) across L1721 and the analytic function fitted to it (dotted line) as a function of radial distance, r , and the visual extinction integrated from the cloud border, A_v . The peak observed at the right end of the cut is due to the plate saturation by the ν Sco star. The LWS positions are marked by squares.

3.2. The radiation field

The ratio $I_{100\mu\text{m}}/N_H$ provides a good measure of the radiation field strength (Bernard et al., 1992, see Fig. 9 in). In Fig. 6, we show the relationship between the IRAS 100 μm surface brightness and the observed column density. In the diffuse part of the cloud ($A_v \leq 0.8$), we observe a good linear correlation between the IRAS 100 μm surface brightness and the column density. The slope $I_{100\mu\text{m}}/N_H$ of this correlation provides an estimate of the radiation field intensity. For a set of clouds in Chamaleon with an opacity comparable to L1721 Boulanger et al. (1998) found a $I_{100\mu\text{m}}/N_H$ ratio of 7.5 ± 2.5 MJy/sr/mag which corresponds to 4 ± 1.3 MJy/sr/ $(10^{21} \text{ cm}^{-2})$. This study provides the reference value for the mean Solar Neighbourhood ISRF (Interstellar Standard Radiation Field). In L1721 we find a slope of 15 ± 4 for the cloud side opposite to ν Sco and 23 ± 4 for the cloud side facing ν Sco (see Fig. 6) which corresponds to 4 and 6 times the ISRF respectively. We emphasize here that the IRAS 100 μm emission profile is relatively insensitive to abundance variations of the small grains (PAHs and VSGs) as shown in Bernard et al. (1992).

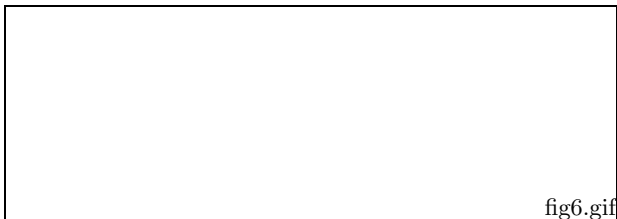


Fig. 6. The 100 μm IRAS surface brightness (a) opposite to ν Sco and (b) facing ν Sco as a function of the column density observed along each line of sight.

The radiation field heating L1721 is the sum of two contributions. The first contribution is from the ν Sco star, which has a luminosity of $6300 L_\odot$ and an effective temperature of 20,000 K. The contribution of ν Sco depends



Fig. 7. Geometry used for modelling L1721. The projected distance of ν Sco to the cloud center is 1.7 pc.

on the position of the star along the line of sight: we reference this position with an angle θ between the sky plane and the line connecting the cloud center to ν Sco (see Fig. 7). Next, the ISRF at this position is likely to be enhanced relative to the mean Solar Neighbourhood ISRF because L1721 is heated by the B and A stars cluster of Upper Scorpius. The Upper Scorpius complex contains a large proportion of stars with effective temperature of less than 20,000 K (de Geus et al., 1989). We use the Mathis et al. (1983) radiation field to represent the mean Upper Scorpius radiation field. This last radiation field is assumed to be isotropic and in the following we call this contribution the *isotropic radiation field*. The radiation field exciting L1721 thus only depends on the distance of ν Sco to the cloud center and on the strength of the Upper Scorpius contribution. The slope of the 100 μm - N_H correlation measures the power absorbed by Big Grains per Hydrogen atom. This power depends on the intensity but also on the spectral distribution of the radiation field. In practice, for a given radiation field intensity at 1000 \AA , the emission of BGs per H atom is 2.5 times larger for the Mathis et al. (1983) radiation field than for a 20,000 K blackbody. We have taken into account this dependence to translate the 100 $\mu\text{m}/N_H$ slopes into χ -values which represent the strength of a radiation field at $\lambda = 1000 \text{ \AA}$ in units of $1.6 \cdot 10^{-3}$ ergs/cm²/sr (Habing, 1968). The radiation field intensity is described in this way because the far-UV photons are more efficient to heat the gas. The strength of the ν Sco radiation field is represented by χ_{sco} and the strength of the *isotropic radiation field* by the factor χ_I . We have considered two cases:

1. $\chi_I = 1$ for the isotropic radiation field and $\chi_{sco} = 12.5$. In that case most of the radiation field strength on both cloud sides is due to ν Sco.
2. The Upper Scorpius isotropic radiation field on L1721 is the dominant radiation field on the cloud side opposite to ν Sco and then $\chi_I = 4$ and $\chi_{sco} = 5$.

A detailed modelling of the dust IR emission in L1721, based on the model of Bernard et al. (1992), is currently underway in our group to discriminate between these two cases. We expect that the case 2 radiation field will propagate more efficiently than the UV light towards the cloud center because of the strong visible component of the radiation field. Also, note that the effects of clumpiness can

affect the penetration of star light inside the cloud. For the line modelling, we select the case 2 to describe the exciting radiation field of L1721. In Sect. 3.4, we will discuss the sensitivity of the gas cooling lines emission to the incident radiation field. In the case 2, the contribution of ν Sco amounts to a mean value of $\chi_{sco} = 5$ for the cloud side facing ν Sco, which corresponds to $\theta = 70^\circ$ for the position of the star. As the far-infrared extinction is small, a very similar $100 \mu m$ emission band profile is expected for $\theta = -70^\circ$. We will see in Sect. 3.4 that $\theta = +70^\circ$ is favoured.

3.3. PDR model

To interpret the gas line emission we make use of the model described in Le Boulrot et al. (1993). In this model a PDR is represented by a semi-infinite plane-parallel slab with an isotropic radiation field incident on the interface. The inputs parameters are (i) χ , the scaling factor for the radiation field, and (ii) the density profile. With these inputs the model solves the chemical and thermal balances starting from the slab edge. The scattering of the radiation by dust grains is treated with the formalism of Flannery et al. (1980) in the plane-parallel case and assumes a mostly forward scattering ($g = \langle \cos \alpha \rangle = 0.6$, where α is the scattering angle). For extinction properties, we use the analytical fit of Fitzpatrick & Massa (1988) to the Galactic average extinction curve. The radiative transfer in the absorption lines of H_2 and CO is treated in detail and the individual line profiles are treated with the prescription of Federman et al. (1979). We use recent gas phase elemental abundances measured in the diffuse interstellar medium: $He/H = 0.1$, $C/H = 1.4 \cdot 10^{-4}$ (Cardelli et al., 1996), and $O/H = 3.19 \cdot 10^{-4}$ (Meyer et al., 1998).

For the photoelectric effect on small dust grains, we adopt the formalism of BT. In particular, our model takes into account the actual spectral distribution of the radiation field to compute the heating rate (Eqs. 1 and 14 of BT). The exponent of the power law size distribution of small grains is -3.5 while the lower and upper limits of the grain radius are 4 and 100 \AA respectively. Larger grains are not included in the computation of the photoelectric heating rate. They have a low photoelectric efficiency due to the large number of collisions the electron must undergo before escaping the grain (Verstraete et al., 1990). The computation of the photoelectric heating assumes that the small grains are graphitic and spherical. Grains with less than 50 C atoms are likely to be planar: these species (PAHs) are less charged and consequently have a higher photoelectric efficiency (BT). However, for a given radiation field, the gain does not exceed 25% (Wolfire et al., 1995): such variations fall within our error bars on the gas cooling lines.

3.4. Spatial distribution of line emission

We now present results of the PDR model for the parameters described in the last three sections. The total strength, $\chi_t = \chi_I + \chi_{sco}$, of the radiation field on the cloud surface ranges from 4 (opposite to ν Sco) to 11 (facing ν Sco). Figs. 8 & 9 describe the chemical stratification and the thermal budget of the plane-parallel model as a function of depth into the cloud. In these figures we have used $\chi = \chi_t = 5$, which corresponds to the mean radiation field received by a particle located on the cloud surface facing ν Sco. We note that the photoelectric effect dominates by far the gas heat budget.

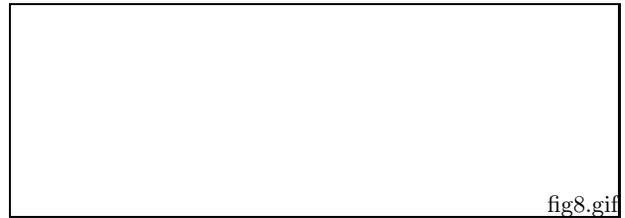


Fig. 8. Variation of the gas temperature, the gas density and the fractional ionization $x = n_e/n_H$ for a plane-parallel PDR model with $\chi = 5$ and the density profile of Sect. 3.1. We also show the H/H_2 and $C^+/C^0/CO$ transitions for the same model. The ν Sco star lies to the left end of the figure.

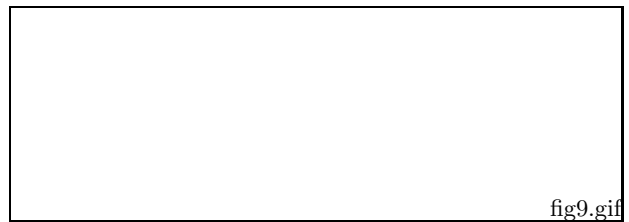


Fig. 9. Main heating and cooling rates for the PDR model ($\chi = 5$).

We now use the PDR model to compute profiles of line fluxes across the cloud which can be compared to the observations. To do this, we approximate the spherical shape of the cloud by a combination of plane-parallel models. This allows us to take into account the variation of the radiation field at the cloud surface and the fact that each line of sight crosses diffuse, warm, interface gas as well as more deeply embedded, colder regions. We thus divide the cloud into angular sectors. The first sector takes up all the cloud side opposite to ν Sco (the area noted *A* in Fig. 7). In addition, six equal sectors are defined on the side facing ν Sco (the area noted *B* in Fig. 7): these sectors are symmetrically distributed with respect to the line connecting ν Sco to the cloud center. To each angular sector is associated one value of χ_t . The three sectors facing

ν Sco on one side of the ν Sco-cloud center line have $\chi_t = 11, 10$ and 9 (going away from the ν Sco-cloud center line). The large sector A opposite to ν Sco receives $\chi_t = \chi_I = 4$. We then run a PDR model for each sector with the density distribution of Sect. 3.1 and the corresponding value of χ_t . The model output is a local line emission rate (J_ν) which only depends on the optical depth measured along a radius from the cloud edge.

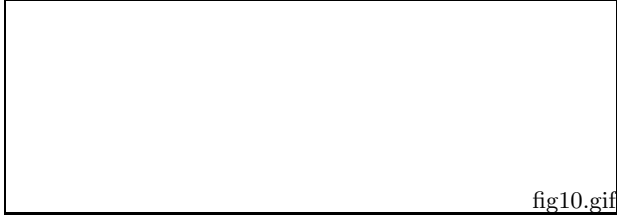


Fig. 10. Geometry used to calculate the line emission profiles intensities. Index k labels the various angular sectors while i labels the A_ν -layers of the PDR models.

The line intensity integrated along a given line of sight is written as (see Fig. 10):

$$I_\nu = \sum_{k,i} \frac{\Lambda_\nu(k,i)}{4\pi} \times l(k,i) \quad (3)$$

In this expression, k labels the angular sectors and i the various layers (defined by the radial A_ν taken from the cloud edge) crossed by the line of sight within an angular sector; $l(k,i)$ is the length in cm of the layer i in the k angular sector on the line of sight. The line cooling rate in erg/s/cm^3 $\Lambda_\nu(k,i)$ is equal to $J_\nu(k,i) \times \beta(i)$ where $J_\nu(k,i)$ is the line emissivity extracted from the PDR model and $\beta(i)$ the escape probability from layer i to the cloud edge along the line of sight. For β , we use the formalism of Tielens & Hollenbach (1985) in their Appendix B with a turbulent Doppler width $\delta v_d = 1$ km/s. We find that the $[\text{C}^+]$ $158\mu\text{m}$ and $[\text{O}^0]$ $63\mu\text{m}$ lines reach an optical depth of 1 at $A_\nu=0.5$ and 0.3 respectively. The H_2 rotational lines are optically thin.

The model line intensity profiles results are compared to the data in Fig. 11. We have put the star at $\theta = +70^\circ$ (Fig. 7). Actually, for $\theta = -70^\circ$ the model line emission is significantly lower due to line opacity. With a dust-to-gas mass ratio of the small grain populations (PAHs and VSGs) constant throughout the cloud and equal to $8.6 \cdot 10^{-4}$, the observed C^+ and O^0 line intensity profiles are not reproduced by the PDR model. Indeed, the $[\text{C}^+]$ $158\mu\text{m}$ and $[\text{O}^0]$ $63\mu\text{m}$ line intensities are underestimated by a factor of about 2 and 3 respectively. The uncertainty on the radiation field, mentioned in Sect. 3.2, amounts to relative error of 40% for C^+ and 70% for O^0 . Such error bars cannot explain the discrepancy between the observed and predicted profiles. Also a higher C and O abundances cannot accommodate this difference, because the fine structure line intensities are practically lin-



Fig. 11. Line emission profiles as observed (solid lines with squares) and predicted by the PDR model as a function of radius and of visual extinction from the cloud edge. The dotted and dashed lines correspond to a calculation with a small dust grain abundance constant throughout the cloud and δv_d equal to 1 km/s and 3 km/s respectively. The model with small dust grain abundance variations and $\delta v_d = 1$ km/s or 3 km/s is represented by the solid and dot-dash lines respectively. The H_2 line cooling has not been observed.

early dependant on the gas phase elemental abundances. Such discrepancies may arise from transfer effects on the emerging cooling lines and/or an underestimated heating rate.

In the PDR model, the non-thermal velocity fields are represented by the turbulent Doppler width δv_d which is added to the thermal width (Tielens & Hollenbach, 1985). This parameter affects the transfer of resonant UV photons through the absorption lines of H_2 and CO and the opacity of the emerging IR cooling lines. We show the result of varying δv_d in Fig. 11: for a reasonable range of δv_d -values, we see that decreasing the opacity of the emerging cooling lines does not account for the observed intensities, in particular $[\text{O}^0]$.

Alternatively, the low intensity of the gas cooling lines in the model may tell us that the gas temperature is too low (see Fig. 8). Indeed, the predicted $[\text{O}^0]$ $63\mu\text{m}$ line emission is very sensitive to the gas temperature because the energy of the transition corresponds to a temperature of 228 K. Thus, another solution to match the data is to increase the heating rate. This latter scales with the UV radiation field intensity (χ), the small grains abundance and the photoelectric efficiency (BT). The band ratios shown in Fig. 12 suggest that the PAHs and VSGs abundance vary across the cloud. In the next subsection we estimate these variations and show that they have an important impact on the emerging gas cooling. We have not attempted to change the abundance of BGs, because as mentioned in the Sect. 3.3, these large grains have a low photoelectric efficiency.

3.5. Abundance variations of the small grains

In this section, we first use the dust brightness profile to quantify the abundance variations of small dust grains. We then include these abundance variations in the PDR model and estimate the corresponding line intensity profiles as in

the last section. Here we test the idea that the discrepancy between the observed and the predicted profiles is due to abundance variations of the small dust grains. Ratios of the brightness profiles of Fig. 4 are presented in Fig. 12.



Fig. 12. Emission ratios of the different dust components as observed (solid lines with squares) and as predicted (solid lines) as a function of radius and of visual extinction from the cloud edge.



Fig. 13. Variation of the interstellar carbon abundance in PAHs (solid line) and VSGs (dotted line) of PDR models as a function of radius and of visual extinction integrated from the cloud border.

We have estimated the abundance variations of small grains from the ratio of PAHs and VSGs emission to that of BGs. A coherent modelling of the dust emission from a spherical cloud (e.g. Bernard et al., 1992, 1993) which includes consistent dust abundance variations is beyond the scope of the present paper. We estimate the model IR emission of dust grains I_{PAH}^{mod} , I_{VSG}^{mod} and I_{BG}^{mod} as follows. The power in the IR emission of the different dust components, $X = [PAH, VSG, BG]$, is equal to the power absorbed, *i.e.*:

$$I_X^{mod} = \left[\frac{X}{H} \right] \times \sum_k \sum_i P_{abs}^X(k, i) \times \frac{n_H(k, i)}{4\pi} \times l(k, i) \quad (4)$$

where

$$P_{abs}^X(k, i) = \int_0^{13.6 \text{ eV}} \sigma_X(E) F_{k,i}(E) dE \quad (5)$$

is the power absorbed in $\text{erg s}^{-1} \text{H}^{-1}$ with σ_X , the absorption cross-section per grain for PAHs, VSGs and BGs. $F_{k,i}(E)$ is the radiation field (in $\text{erg s}^{-1} \text{cm}^{-2} \text{eV}^{-1}$), found from the transfer prescriptions described in Sect. 3.3, and $n_H(k, i)$ the density in each cloud zone characterised by the index k and i (see Fig. 10). For the BGs we take the cross section of Désert et al. (1990), for PAHs we use Verstraete & Léger (1992) and Draine & Lee (1984)

Table 1. Average power radiated per hydrogen atom by gas coolants and small dust grains towards L1721

Species	Power ^a :	Observed	Theoretical
[C ⁺] 158 μm		1.2	1
[O ⁰] 63 μm		0.34	0.32
H ₂			0.27
Total gas cooling		1.81 ^b	1.59
$I_{PAH} + I_{VSG}$		78	54
ϵ_{PE}		0.023	0.029

^a In $10^{-25} \text{ erg s}^{-1} \text{H}^{-1}$

^b Including the H₂ contribution as estimated from the model

for VSGs. In the ISRF, PAHs absorb $2.3 \cdot 10^{-27} \text{ Watt/C}$ whereas graphitic VSGs only absorb $1.7 \cdot 10^{-27} \text{ Watt/C}$. Formula (4) can then be inverted to infer the dust abundance (C/H in PAHs and VSGs) as a function of cloud radius. The resulting abundance profiles are presented in Figs. 11, 12 and 13. The abundance of PAHs has to be multiplied by ~ 5 in the $[0.25 < A_v \leq 0.45]$ -layer to account for the observed I_{PAH}/I_{BG} ratio. Similarly, the VSGs abundance must be multiplied by ~ 2 in the $[A_v \geq 0.75]$ -layer in order to reproduce the observed I_{VSG}/I_{BG} emission ratio.

Including these abundance variations in the PDR modelling, we obtain the result displayed in Fig. 11. The corresponding line intensities are higher: the C⁺ and O⁰ lines emission are increased by a factor about 1.5 and 3 respectively. The discrepancy at the center of the cloud between the observed and predicted line profiles may result from uncertainties in the radiation field, the radiation transfer, or the photoelectric efficiency and from our rough estimate of the small dust grain abundance profiles. In the present PDR modelling we have not attempted to include changes in the UV extinction curve associated with the small dust grain abundance variations because recent observations (Boulanger et al., 1994) have questioned the contribution of small dust grains to the extinction curve adopted in the current dust models (Désert et al., 1990; Dwek et al., 1997, e.g.). In any case, exploring a range of far-UV to visible extinction ratio (from 5 to 10 at 1000 Å) we find the cooling lines to vary by less than 50 %. We therefore conclude, that the observed intensity profile of the main gas cooling lines can only be reproduced if the abundance of PAHs is significantly increased. This result

illustrates the dominant role of the smallest dust grains in the gas heating. It also shows that the model photoelectric efficiency is close to its actual value. In Table 1, the values of the power radiated by gas coolants and small dust grains as observed and modelled are listed.

4. Dust photoelectric efficiency

Using our model estimate of the H_2 cooling, we can now estimate the photoelectric efficiency by comparing the observed dust and gas emissions. A relationship is theoretically expected between the main cooling rates and the dust emission. Indeed, a dust grain exposed to a stellar radiation field dissipates the energy it absorbs mostly as IR emission. A small fraction, ϵ , of the energy absorbed is channelled to the gas by the photoelectric effect. The heating efficiency of this latter process is defined as

$$\epsilon = \frac{P_{PE}}{P_{abs}} \quad (6)$$

where P_{abs} is the total power absorbed by the dust grains and P_{PE} is the power given to the gas through the photoelectric effect. For a gas in thermal balance, the gas heating and cooling rates are equal. In the L1721 PDR, the gas heating is dominated by the photoelectric effect. Assuming thermal balance the photoelectric heating is thus roughly equal to the total cooling rate. As long as the opacity of the emerging cooling lines is small, we can replace P_{PE} by the total gas cooling line emissions I_Λ . Moreover, as the power conveyed by the photoelectric effect is much smaller than the absorbed power ($\epsilon \sim$ a few 10^{-2}), the latter power is well approximated by the dust IR emission. Finally, ϵ can be observationally defined as:

$$\epsilon \simeq \frac{I_\Lambda}{I_{dust}} \quad (7)$$

where I_{dust} is the total dust IR emission.

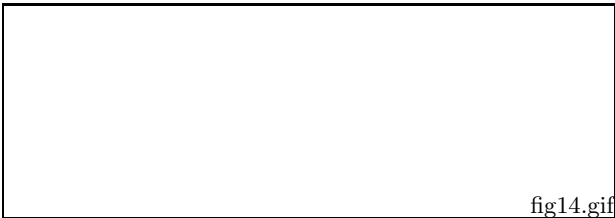


Fig. 14. *Upper panel: intensities in the C^+ and O^0 lines measured by LWS, and cooling in the H_2 rotational lines (see Sect. 3.3.4). Lower panel: The total gas cooling, $I_\Lambda = I_{C^+} + I_{O^0} + I_{H_2}$ with 3σ error bars (solid line with crosses) and as derived from the dust IR emission: (i) $I_\Lambda^d = 0.03 \times I_{PAH} + 0.01 \times I_{VSG} + 0.001 \times I_{BG}$ (solid line) and (ii) $I_\Lambda^{BG} = 0.001 \times I_{PAH} + 0.001 \times I_{VSG}$ 01h 1*

that the ϵ_{mod} -values are within 30% of those of ϵ_{obs} . The shape of the ϵ_{mod} -profile can be understood as follows. While penetrating into the cloud ($r \geq 0.3$ pc), the UV radiation is attenuated and the average grain charge (positive) decreases; consequently, ϵ_{mod} increases because of the weaker Coulomb barrier for the ejection of electrons from the grain (BT). Towards the center of the cloud ($r \leq 0.3$ pc), the photoelectric efficiency decreases. This trend is the combination of two effects. On the one hand, the opacity of the cloud center to UV photons is larger than for visible photons: since the photoelectric effect is produced mostly by UV photons, ϵ_{mod} diminishes towards the cloud center. On the other hand, the ϵ_{mod} -drop at $r \leq 0.3$ pc also reflects the behaviour of the n_{PAH}/n_{VSG} ratio (see Fig. 12). Comparing ϵ_{mod} and ϵ_{obs} in detail, we see that the efficiency values at the cloud boundary are quite comparable. Moving into the cloud, ϵ_{obs} is systematically lower than ϵ_{mod} . Also, the ridge and trough of the ϵ_{mod} -profile are somewhat shifted with respect to ϵ_{obs} . These discrepancies probably result from the simplified geometry and radiation transfer we adopted for the L1721 cloud, as well as the uncertainty in the spectral distribution of the exciting radiation field (see Sect. 3.2). In this latter case, a detailed modelling of the dust infrared emission is warranted in order to consistently derive the exciting radiation field and the dust abundance profiles in the L1721 cloud.

5. Conclusion

We study the gas thermal balance and the dust IR emission across L1721 a nearby, isolated molecular cloud heated by the ν Sco star and by the BA star association of Upper Scorpius. The cooling of the gas is obtained with ISO-LWS measurements of the major cooling lines, $[C^+]$ $158\mu m$ and $[O^0]$ $63\mu m$. The dust IR emission is traced with IRAS data.

We model the gas cooling lines with an updated version of the photodissociation region model of Le Bourlot et al. (1993). The input physical conditions in this modelling are the density profile and the exciting radiation field. The density profile of the L1721 cloud is deduced from visual extinction data (A_v at the center is ~ 3). The exciting radiation field is estimated to be $\chi = 5$ to 10 times the radiation field of the Solar Neighbourhood from the ratio of dust emission to gas column density.

The spatial correlation between the gas cooling lines and the IR emission of small grains (PAHs and VSGs of radii ≤ 100 Å) confirms the theoretical expectation that the gas heat budget, in the less excited PDRs, is dominated by the photoelectric effect on small grains. The photoelectric efficiency measured from the ratio of the total gas cooling to the dust IR emission is in the range 2 to 3% in good agreement with current theoretical models (Bakes & Tielens, 1994; Weingartner & Draine, 2001).

Moreover, we find that the gas cooling lines of the L1721 cloud cannot be explained if the abundance of small grains

is kept constant across the cloud, equal to the abundance of the diffuse ISM. Rather, as indicated by the IRAS band ratios, our PDR model results matches the gas cooling line observations when the abundance of PAHs is enhanced by a factor of 5 towards the cloud center.

Acknowledgements. We are grateful to L. Cambr esy for providing us the extinction map of L1721. We also thank E. Caux and W.T. Reach for their help with the LWS data reduction.

References

- Bakes, E. L. O & Tielens, A. G. G. M. 1994, *ApJ*, 427:822.
 Bernard, J. P, Boulanger, F, Desert, F. X, & Puget, J. L. 1992, *A&A*, 263:258.
 Bernard, J. P, Boulanger, F, & Puget, J. L. 1993, *A&A*, 277:609.
 Bernard, J. P, Boulanger, F, D esert, F. X, Giard, M, Helou, G, & Puget, J. L. 1994, *A&A*, 291:L5.
 Boulanger, F, Falgarone, E, Puget, J. L, & Helou, G. 1990, *ApJ*, 364:136.
 Boulanger, F, Prevot, M. L, & Gry, C. 1994, *A&A*, 284:956.
 Boulanger, F, Abergel, A, Bernard, J. P, Burton, W. B, D esert, F. X, Hartmann, D, Lagache, G, & Puget, J. L. 1996a, *A&A*, 312:256.
 Boulanger, F, Reach, W. T, Abergel, A, Bernard, J. P, Cesarsky, C. J, Cesarsky, D, D esert, F. X, Falgarone, E, Lequeux, J, Metcalfe, L, Perault, M, Puget, J. L, Rouan, D, Sauvage, M, Tran, D, & Vigroux, L. 1996b, *A&A*, 315:L325.
 Boulanger, F, Bronfman, L, Dame, T. M, & Thaddeus, P. 1998, *A&A*, 332:273.
 Cambr esy, L. 1999, *A&A*, 345:965.
 Cardelli, J. A, Meyer, D. M, Jura, M, & Savage, B. D. 1996, *ApJ*, 467:334.
 Caux, E & Gry, C. Iso lws spectroscopy of the diffuse interstellar medium. In *The Far Infrared and Submillimetre Universe*, page 67, 1997.
 Clegg, P. E, Ade, P. A, Armand, C, Baluteau, J. P, & Barlow, M. J. et al. 1996, *A&A*, 315:L38.
 de Geus, E. J, DeZeeuw, P. T, & Lub, J. 1989, *A&A*, 216:44.
 D esert, F. X, Boulanger, F, & Puget, J. L. 1990, *A&A*, 237:215.
 Draine, B. T & Lee, H. M. 1984, *ApJ*, 285:89.
 Dwek, E, Arendt, R. G, Fixsen, D. J, Sodroski, T. J, Odegard, N, Weiland, J. L, Reach, W. T, Hauser, M. G, Kelsall, T, Moseley, S. H, Silverberg, R. F, Shafer, R. A, Ballester, J, Bazell, D, & Isaacman, R. 1997, *ApJ*, 475:565.
 Federman, S. R, Glassgold, A. E, & Kwan, J. 1979, *ApJ*, 227:466.
 Fitzpatrick, E. L & Massa, D. 1988, *ApJ*, 328:734.
 Flannery, B. P, Roberge, W, & Rybicki, G. B. 1980, *ApJ*, 236:598.
 Habing, H. J. 1968, *Bull. Astron. Inst. Netherlands*, 19:421.
 Hollenbach, D. J & Tielens, A. G. G. M. 1999, *Reviews of Modern Physics*, 71:173.
 Hollenbach, D. J, Takahashi, T, & Tielens, A. G. G. M. 1991, *ApJ*, 377:192.
 Kemper, C, Spaans, M, Jansen, D. J, Hogerheijde, M. R, vanden Dishoeck, E. F, & Tielens, A. G. G. M. 1999, *ApJ*, 515:649.
 Kessler, M. F, Steinz, J. A, Anderegg, M. E, Clavel, J, Drechsel, G, Estaria, P, Faelker, J, Riedinger, J. R, Robson, A, Taylor, B. G, & Ximenez De Ferran, S. 1996, *A&A*, 315:L27.

- Le Bourlot, J, Pineau Des Forets, G, Roueff, E, & Flower, D. R. 1993, *A&A*, 267:L233.
- Lynds, B. T. 1962, *Astrophysical Journal Supplement Series*, 7:L1.
- Mathis, J. S, Mezger, P. G, & Panagia, N. 1983, *A&A*, 128:212.
- Meyer, D. M, Jura, M, & Cardelli, J. A. 1998, *ApJ*, 493:222.
- Tielens, A. G. G. M & Hollenbach, D. 1985, *ApJ*, 291:722.
- Verstraete, L & Léger, A. 1992, *A&A*, 266:513.
- Verstraete, L, Léger, A, D'Hendecourt, L, Defourneau, D, & Dutuit, O. 1990, *A&A*, 237:436.
- Weingartner, J. C & Draine, B. T. 2001, *astro-ph/9907251* submitted to *ApJ*.
- Wolfire, M. G, Hollenbach, D, McKee, C. F, Tielens, A. G. G. M, & Bakes, E. L. O. 1995, *ApJ*, 443:152.
- Wright, E. L, Mather, J. C, Bennett, C. L, Cheng, E. S, & Shafer, R. A. et al. 1991, *ApJ*, 381:200.

This figure "fig1.gif" is available in "gif" format from:

<http://arxiv.org/ps/astro-ph/0104150v1>

This figure "fig2.gif" is available in "gif" format from:

<http://arxiv.org/ps/astro-ph/0104150v1>

This figure "fig3.gif" is available in "gif" format from:

<http://arxiv.org/ps/astro-ph/0104150v1>

This figure "fig4.gif" is available in "gif" format from:

<http://arxiv.org/ps/astro-ph/0104150v1>

This figure "fig5.gif" is available in "gif" format from:

<http://arxiv.org/ps/astro-ph/0104150v1>

This figure "fig6.gif" is available in "gif" format from:

<http://arxiv.org/ps/astro-ph/0104150v1>

This figure "fig7.gif" is available in "gif" format from:

<http://arxiv.org/ps/astro-ph/0104150v1>

This figure "fig8.gif" is available in "gif" format from:

<http://arxiv.org/ps/astro-ph/0104150v1>

This figure "fig9.gif" is available in "gif" format from:

<http://arxiv.org/ps/astro-ph/0104150v1>

This figure "fig10.gif" is available in "gif" format from:

<http://arxiv.org/ps/astro-ph/0104150v1>

This figure "fig11.gif" is available in "gif" format from:

<http://arxiv.org/ps/astro-ph/0104150v1>

This figure "fig12.gif" is available in "gif" format from:

<http://arxiv.org/ps/astro-ph/0104150v1>

This figure "fig13.gif" is available in "gif" format from:

<http://arxiv.org/ps/astro-ph/0104150v1>

This figure "fig14.gif" is available in "gif" format from:

<http://arxiv.org/ps/astro-ph/0104150v1>

This figure "fig15.gif" is available in "gif" format from:

<http://arxiv.org/ps/astro-ph/0104150v1>